LASER & PHOTONICS REVIEWS
www.lpr-journal.org

Megahertz-Rate Widely Tunable Fiber Filters Enabled by $LiNbO_3$ Actuators

*Hongwei Tong, Yifeng Xiong, Ziheng Wang, Zhaoxian Chen, Zhenhui Qin, Zhanqi Xing, Zhechun Lu, Haotian Ding, Ye Chen, and Fei Xu**

High-speed optical fiber tunable filters are crucial for wavelength sweeping and spectral analysis, but reliably capturing transient events in submicrosecond-scale, such as blasting and seismic waves, remains a challenge. Conventional piezoelectric transducer (PZT) typically achieves tuning rates of 10 kHz level due to its relatively low mechanical quality factor (Q factor) and high dielectric loss, limiting its performance in high-speed applications. Here a fast-tuned, large-range filter is demonstrated by integrating a fiber Fabry-Perot (FP) cavity onto a multilayer all-lithium niobate ($LiNbO_3$, Y-cut 163-degree) actuating structure. Leveraging the low dielectric loss, high electromechanical coupling coefficients (EMCC) and mechanical Q factor of $LiNbO_3$, along with the lightweight integration optimization, a high tuning frequency of ≈1.52 MHz and a tuning range of ≈20 nm are achieved, while maintaining high filtering fineness and low optical loss. The device's overall performance, particularly its loaded tuning frequency, represents a significant improvement over previously reported works. The alignment-free, non-adhesive assembly approach of device produces stable response, effectively eliminates the need for hysteresis compensation, enabling highly accurate, submicrosecond-scale spectra monitoring in fiber demodulation systems. This study presents a competitive solution for high-speed demodulation and is essential for advancing fiber sensing technologies in applications involving transient event measurements.

1. Introduction

The monitoring of light spectra in fiber has been widely applied across various fields, from communications[1,2] to advanced sensing technologies, including medical diagnostics[3,4] and structural health monitoring.[5,6] However, the high-speed spectra demodulation has been a long-standing challenge, particularly in extreme conditions such as blasting and seismic waves,[7,8] fatigue strength testing of materials,[9–11] where test frequencies even exceed 100 kHz. Consequently, it is imperative for the demodulation rate to reach megahertz (MHz) levels for more detailed analysis.

Among the various fiber spectral demodulation strategies, the spectral scanning method based on tunable Fabry Perot (FP) fiber filters is frequently utilized, with most systems constructed using piezoelectric transducer (PZT) actuator.[12,13] However, due to the relatively high dielectric loss[14] and low mechanical quality factor (Q factor)[15,16] of PZT, these systems suffer from low energy conversion efficiency, high mechanical loss under high-frequency modulation, and issues like thermal effect,[17,18] frequency drift,[19] nonlinear behavior,[20] and fatigue failure,[10,11] which limits the demodulation rates to typically 10 kHz-level.[21,22] Additionally, the hysteresis and creep characteristics inherent in PZT can significantly impact the precision and repeatability of the demodulation system,[23] while compensation schemes add complexity and cost. Alternative piezoelectric materials for actuator, such as barium titanate,[24] show promising piezoelectric performance. However, actuators fabricated from these materials often exhibit inherent limitations in aspects such as driving voltage, tuning rate, operating temperature, and integration capabilities. (see Table S1, Supporting Information for details). What's more, the lack of effective integration solutions with optical fibers limits their full potential. Inadequate assembly strategies increase load quality and mechanical damping, reducing the overall stiffness of the piezoelectric device, which negatively impacts both resonance frequency and strength.[25,26] Therefore, there are three critical aspects must be addressed: i) the development of a high-performance piezoelectric actuator platform capable of achieving both high frequency and resonant intensity; ii) robust integration of piezoelectric materials within all-fiber devices; and iii) the effective realization of the material's high-frequency potential through carefully design and assembly.

H. Tong, Y. Xiong, Z. Wang, Z. Chen, Z. Qin, Z. Xing, Z. Lu, H. Ding, Y. Chen, F. Xu
National Laboratory of Solid State Microstructures
College of Engineering and Applied Sciences
Nanjing University
Nanjing 210023, China
E-mail: feixu@nju.edu.cn
H. Tong, Y. Xiong, Z. Wang, Z. Chen, Z. Qin, Z. Lu, H. Ding, F. Xu
Collaborative Innovation Center of Advanced Microstructures
Nanjing University
Nanjing 210093, China

The ORCID identification number(s) for the author(s) of this article can be found under https://doi.org/10.1002/lpor.202500835

DOI: 10.1002/lpor.202500835

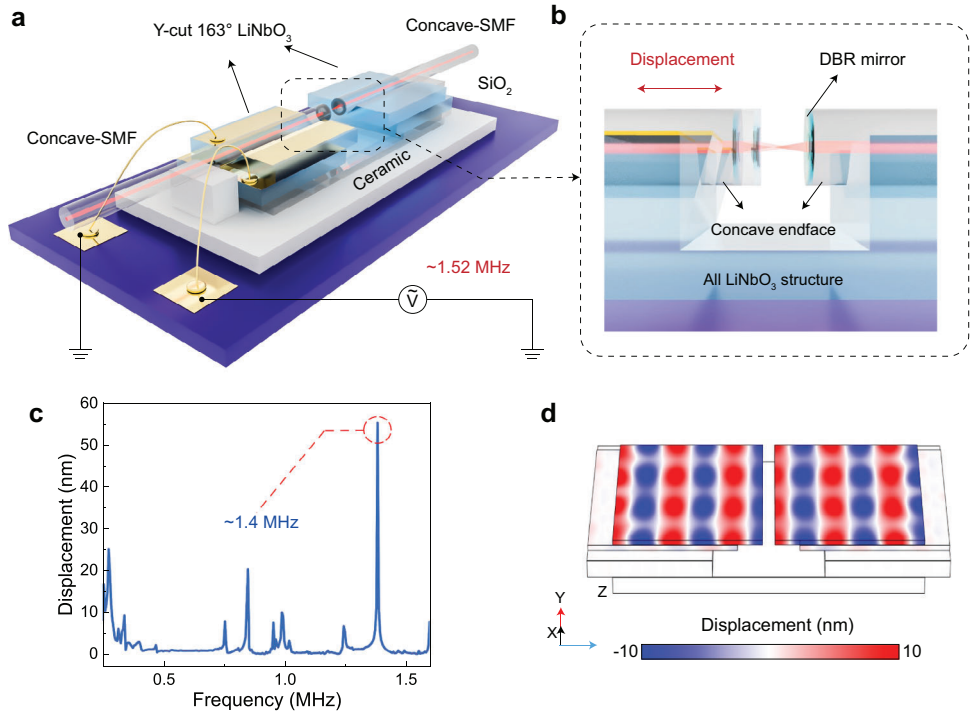

Figure 1. Mechanism of the fast-tuned $LiNbO_3$-actuated OFFPF. a) Schematic diagram of the device structure. A pair of concave optical fibers forms an FP cavity, integrated using slots etched on the multilayer all-$LiNbO_3$ structure driven by a high-frequency AC source. b) Detailed illustration of the tuning mechanism of the device. The fiber cavity length is modulated by the displacement of the actuating $LiNbO_3$, with the maximum displacement occurring at the resonant frequency of 1.52 MHz. c) Simulation of the resonant response of $LiNbO_3$ actuator at different frequencies along the length direction. d) The shear vibration mode near 1.4 MHz.

In this study, we demonstrated a high-speed, highly repeatable, and wide-range tunable optical fiber FP filter (OFFPF) using a lithium niobate ($LiNbO_3$) actuator (Y-cut 163-degree), which offers excellent piezoelectric properties[27] at high frequencies, such as high electromechanical coupling coefficients (EMCC),[28] mechanical Q factor, and shear vibration intensity. With minimal creep and hysteresis,[29,30] the OFFPF achieves high repeatability and linearity of about 0.998. To enhance stability and high-frequency performance, we eliminated additional fiber-aligned components to reduce load quality and used high-elastic modulus connection materials to enhance actuator stiffness. This non-adhesive, alignment-free assembly approach, along with a carefully designed actuator and integration scheme, results in a $LiNbO_3$-actuated OFFPF (LNOFFPF) with a tuning rate of ≈1.52 MHz, a dynamic tuning range of ≈20 nm at 60 Vpp, and a finesse above 490, eliminating the need for external hysteresis and creep compensations. We achieved dynamic spectral measurements using the LNOFFPF to monitor sub-microsecond varied spectral signals from an actuated tunable FP filter and detect instantaneous stress variations in a fiber Bragg grating (FBG), highlighting its high-speed demodulation capability in practice applications. Our device, noted for its high tuning rate and repeatability, offers a competitive solution for high-speed demodulation and is essential in transient event measurements.

2. Results

2.1. Design of the Device Structure

Owing to their outstanding piezoelectric properties, $LiNbO_3$ crystals are commonly utilized in the fabrication of photo-elastic modulators,[26] ultrasonic transducers,[27,31] and surface acoustic wave filters.[32,33] However, due to challenges in processing and integration,[34–36] $LiNbO_3$ has rarely been employed directly in all-fiber devices as piezoelectric crystals. It was only in our previous work that $LiNbO_3$ wafers were first employed to actuate fiber FP filters.[37]

The key to enhancing the stability and tuning speed of the $LiNbO_3$-actuated OFFPF lies in optimizing its configuration and assembly process, as presented in **Figure 1**a. The $LiNbO_3$ actuator structure consists of four layers of $LiNbO_3$, arranged from bottom to top (Figure 1b). The two bottom substrate layers are each 1 mm thick, with two chips in the second layer providing support to form a cantilever structure with the upper chips. The top two layers, each ≈0.3 mm thick, are coated with gold film to function as electrodes. The top wafer, acting as a piezoelectric layer, designed to be 12 mm in length and 10 mm in width, with a slot on its surface fabricated by a wafer dicing machine. A pair of concave optical fibers form an FP cavity within the slot. When an electric field is applied in the thickness direction, the Y-cut

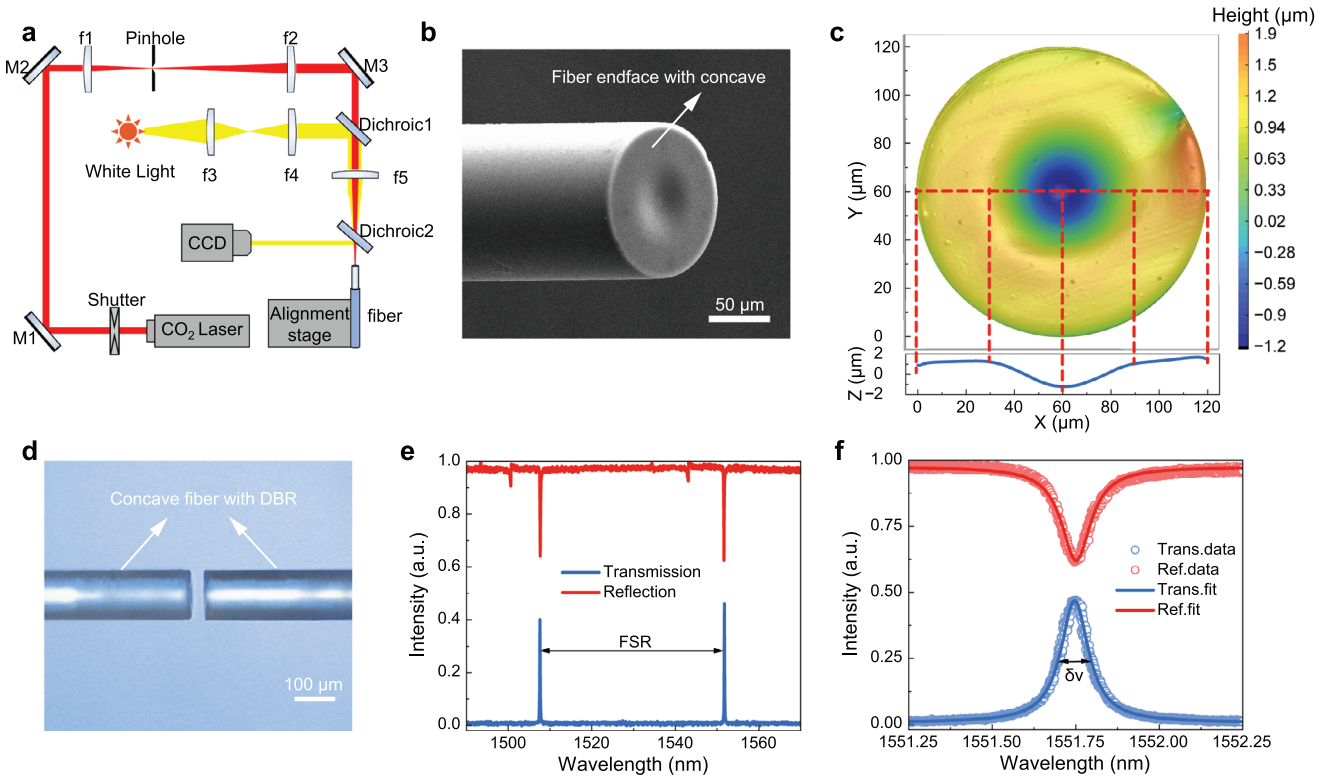

Figure 2. High-performance fiber FP cavity. a) Schematic diagram of CO_2 laser processing system. b) SEM image of concave fiber. c) Surface morphology of concave fiber end face measured by white light interference method. d) Microscopic image of precisely aligned concave fiber FP cavity. e) Measured transmission and reflection spectra of the concave fiber FP cavity, corresponding FSR in length to 44.15 nm. f) Close-up view of the peaks near 1550 nm, corresponding linewidth in length to 0.09 nm.

163-degree $LiNbO_3$ chip experiences shear deformation, causing a change in the length of the FP cavity and thereby tuning the output wavelength of the filter. To analyze the resonant response of the actuator at high frequencies, we performed a finite element simulation on the vibration intensity and displacement distribution of the device (see Supporting Information for details). The Figure 1c reveals a resonance peak near 1.4 MHz, corresponding to a transverse shear mode as shown in Figure 1d.

While the simulation indicates that the $LiNbO_3$ actuator possesses the potential for high-frequency resonance, its effective release in a fiber FP tunable filter depends on the integration and assembly of the actuator with the fiber FP cavity. Fiber alignment components, such as ceramic ferrule, may increase the load quality on the actuator and thus reduce the resonant frequency.[38,39] To address this, we aligned the fiber using a slot etched into the $LiNbO_3$ surface (see Figure S3, Supporting Information for details). Unlike other optical fiber devices rely on adhesives such as ultraviolet glue or epoxy resin, which can affect the stiffness of the actuator and reduce the resonant intensity,[40] we used borosilicate glass powder with a low thermal expansion coefficient (TEC) as the assembly material. The piezoelectric layer was directly bonded to the substrate under high temperature, and the fiber was welded to the actuator using a carbon dioxide (CO_2) laser (see Figure S4, Supporting Information for details). Additionally, the multilayered $LiNbO_3$ structure with identical crystalline orientation solves the fragmentation problem that is caused by the TEC mismatch between the piezoelectric layer and the substrate layer during bonding. Our strategy eliminates the need for alignment components and adhesives, enabling a non-adhesive assembly and alignment-free approach that realize high-frequency tuning.

2.2. High-Performance Dual-Fibers FP Cavity

The fabrication of high-performance fiber FP cavities is of great importance for LNOFFPF, as it directly impacts the filter bandwidth and insertion loss. The concave fiber FP cavities are designed to be insensitive to variations in ambient temperature and humidity. Coated with a ≈99% high-reflectivity dielectric film, the concave cavity further reduces the spot size of the resonant cavity mode (see Figure S6, Supporting Information for details). This approach effectively minimizes in-cavity loss, such as diffraction loss, thereby significantly increasing the finesse to several hundred.

As illustrated in **Figure 2**a, we developed a CO_2 laser processing system to fabricate concave fiber FP cavities, allowing for real-time microscopic observation during fiber endface processing (see Figure S4, Supporting Information, for details). Figure 2b presents a scanning electron microscope image of a concave optical fiber that we prepared, showing a clear pit at the center of the endface following CO_2 laser irradiation. To measure the curvature radius and depth, a white light interferometer (Spanish company SENSOFAR) was employed, as shown in Figure 2c. The fabricated fiber exhibits a concave surface with a diameter

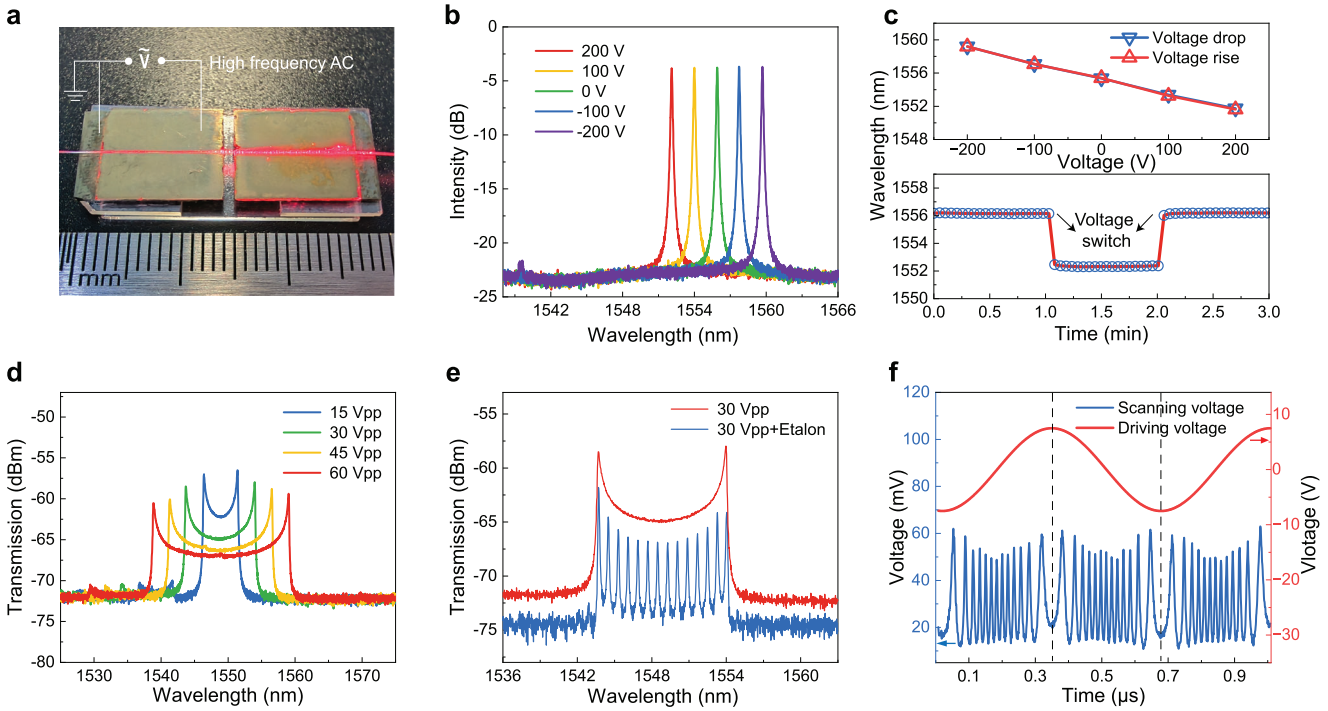

Figure 3. Characteristics of $LiNbO_3$-actuated OFFPF. a) Physical diagram of the LNOFFPF sample with a ruler under it. b) Transmission spectra of OFFPF with different direct current (DC) voltages applied to $LiNbO_3$ actuator. c) The hysteresis curves and Creep test results of the LNOFFPF, indicate a nonlinear error of about 0.2% and minimal fluctuation of about ±0.03 nm during tuning. (d) Transmission spectra of the OFFPF with different alternating current (AC) voltages under 1.52 MHz applied to the $LiNbO_3$ actuator. e) Output spectrum of the LNOFFPF connected with FP etalon. f) The time-domain diagram obtained after the spectral signal in (e) is input to the PD.

of 50 μm, a depth of 2.5 μm, and a curvature radius of approximately 127 μm, as determined by fitting the bottom profile of the concave surface. Figure 2d shows a microscopic view of a concave fiber FP cavity aligned on a displacement stage. The transmission spectrum of this cavity, shown in Figure 2e, was measured by frequency sweep methods. A frequency sweep laser was used as the light source, with a sweep speed set to 1 nm/s and a wavelength range of 1470 nm-1570 nm. A photodetector and an oscilloscope were used to acquire the spectrum signal. The measurement results reveal a free spectral range (FSR) of approximately 44.15 nm, with a linewidth ($\delta\nu$) of around 0.09 nm (Figure 2f). The finesse of the cavity (expressed as $F = \mathrm{FSR}/\delta\nu$) is calculated to be 490, and the optical loss is ≈3.3 dB, exhibiting a significant improvement compared to traditional lens-fiber FP cavities.

2.3. MHz-Rate Tuning of the $LiNbO_3$-Actuated FP Tunable Filter

After integrating the fiber FP concave cavity and the $LiNbO_3$ actuator into the LNOFFPF, we conducted a series of tests to evaluate its tuning performance using the assembled device shown in **Figure** 3a. The full width at half maxima (FWHM) of the device's transmission peak is approximately 0.09 nm, with an optical loss of ≈3.72 dB (see Figure S1,Supporting Information). The FSR of the filter is about 27.2 nm, resulting in a calculated finesse of ≈302. Note that, the finesse is slightly lower compared to the concave fiber FP cavity directly aligned on a displacement stage due to slight fiber alignment errors in the on-chip slots.

We first investigated the static modulation performance of the device. As depicted in Figure 3b, when the DC voltage is adjusted from 200 V to −200 V, the transmission peak wavelength of the filter experiences a redshift, moving from ≈1552.1 nm to ≈1559.7 nm, with a wavelength tuning rate of approximately 1.9 nm/100 V. The static tuning range is limited by the piezoelectric constant of $LiNbO_3$. However, at the resonant frequency of 1.52 MHz, the tuning range is significantly enhanced due to the resonant intensity enabled by the high mechanical Q factor of the $LiNbO_3$ actuator (see Figure S1, Supporting Information, for details). The hysteresis loop of the LNOFFPF in static tuning, shown in the top panel of Figure 3c, demonstrates a high linearity of about 0.998 and remarkable congruence between the voltage-up and voltage-down response curves, ensuring repeatability and high positioning accuracy of the tunable filter. We also investigate the creep behavior of the tunable filter, as shown in the bottom panel of Figure 3c, when the driving voltage alternates between 0 and 200 V, the transmission spectrum of LNOFFPF first experiences a 1.9 nm blue shift and then a 1.9 nm red shift. After each voltage switch, the voltage is held constant for 1 min, during which the spectrum fluctuates by only approximately ± 0.03 nm, demonstrating low creep and high stability of device.

Then, we utilized a photodetector and spectrometer to evaluate the device's dynamic response (experimental setup in Figure S1a, Supporting Information). As shown in Figure S1c (Supporting Information), the filter exhibits a relatively substantial response around 1.52 MHz, which closely matches the resonance frequency predicted in the simulation in Figure 1c. The slight

frequency discrepancies might be attributed to minor size errors during the filter manufacturing process. We set the driving voltage frequency of LNOFFPF to 1.52 MHz and employed a spectrometer to measure its output spectra at various voltages. Since the scanning speed of the spectrometer is much slower than the tuning speed of the filter, the spectra display overlaps of optical signals at different wavelengths. As shown in Figure 3d, when the driving AC voltage values are set to 15 Vpp, 30 Vpp, 45 Vpp, and 60 Vpp, the tuning ranges of the device are approximately 5 nm, 10 nm, 15 nm, and 20 nm, respectively, exhibiting an excellent linear relationship with the voltage value. This relatively large tuning ability is attributed to the actuator's structural design (see Supporting Information for details) and the careful assembly process.

Notably, the spectral transmission contrast decreases inversely with applied voltage magnitude in the dynamic tuning mode. This stems from the direct proportionality between wavelength tuning rate and tuning range at fixed frequency. Due to the spectrometer photodetector's finite response time, detected intensity at each wavelength depends on incident light dwell time. Consequently, higher tuning rates of the LNOFFPF result in smaller intensity and a concomitant decrease in overall transmission contrast. Additionally, the spectral intensity at the central of the scanning range is lower than that at either side due to the highest changing rate in the sinusoidal signal at the mid-value, which the spectrometer's scanning speed cannot fully capture. Employing photodetectors with higher response rates would help mitigate the decrease in transmission contrast under dynamic tuning mode and the intensity drop at the central wavelength.

To measure the dynamic tuning range in the time domain as well, we connected an FP etalon with a 125 GHz FSR to the output end of the LNOFFPF. The LNOFFPF operated at a tuning frequency of 1.52 MHz and an AC voltage of 30 Vpp. The output of the etalon was connected to both the spectrometer and photodetector. As shown in Figure 3e, the spectrometer detected about 13 FSR of the etalon within the scanning range, indicating the dynamic tuning range of the LNOFFPF under these conditions is approximately 10 nm. Figure 3f presents the time-domain characteristics acquired from the PD signal output to the oscilloscope. The time-domain signal intensity variations align with the dynamic spectrum behavior of the filter, confirming that the dynamic tuning range can also be measured in the time domain. Due to the reciprocating amplitude scanning within the sinusoidal signal cycle, two sets of symmetrical time-domain signals are observed in one cycle. Therefore, the scanning frequency of LNOFFPF can also be considered as 3.04 MHz.

2.4. High-Speed Spectra Monitoring with Device

In the context, we have demonstrated the high-speed tuning performance of the LNOFFPF under high-frequency AC voltages by measuring both spectral and time-domain signals. We first used it to measure a dynamic spectral signal that varied at a fixed frequency to verify its demodulation capabilities. A reference tunable fiber FP filter, with FWHM of about 0.12 nm, was used to produce a spectral signal with a tuning frequency of 25 kHz and a tuning range of approximately 6.3 nm. To comprehensively cover the spectral signal tuning range, we set the scanning range of LNOFFPF to be slightly larger than 6.3 nm by applying a 1.52 MHz AC signal with voltage of approximately 19 Vpp, corresponding to a scanning range of about 6.4 nm (Figure S2, Supporting Information).

We then input the scanned optical signal to the photodetector and use a 2 GHz-rate data acquisition system to collect the voltage signal output by the photodetector (see Figure S5, Supporting Information, for details). **Figure** 4a shows the driving voltage signal of the reference OFFPF (red curve, 25 kHz) and the LNOFFPF (orange curve, 1.52 MHz). It can be observed that the transmission peak signal of the reference OFFPF appears twice in succession during each cycle of the sinusoidal voltage driving the LNOFFPF. This is due to the sinusoidal voltage scanning back and forth within each cycle. Since the wavelength of the measured spectral signal changes rapidly, the distance between adjacent peak signals detected by PD during each sinusoidal period also changes (blue curves in Figure 4b). As shown in Figure 4a, this distance increases to a certain extent before starting to decrease until it returns to its original position, completing one full modulation cycle of the sinusoidal voltage signal driving the reference OFFPF. The spectral signal obtained after segmentation and calculation is shown as the red curve in Figure 4c, in which the demodulated variation range (≈6.3 nm) and frequency (25 kHz) of the spectral signal is consistent with the driving conditions of the reference OFFPF, indicating that the LNOFFPF we designed can effectively demodulate dynamic spectral signals. Notably, the mean wavelength interval between consecutive data points is approximately 0.12 nm and the mean-time interval is only ≈0.33 μs (Figure 4e), corresponding to twice the tuning frequency of 1.52 MHz due to the sinusoidal voltage scanning back and forth in a cycle. The maximum and minimum values of the sinusoidal voltage correspond to the two ends of the LNOFFPF scanning range. Therefore, during the rising and falling processes of the sinusoidal voltage, the LNOFFPF performs one scan on the sample respectively. Both scans take half of the sinusoidal signal period, so the actual interval for data extraction is 0.33 microseconds.

In addition, we also used the LNOFFPF to demodulate a high-speed transient event in a commercial FBG sensor with a bandwidth of ≈0.23 nm. The FBG is connected to a 15 g mass object, and the object's freely fall results in a transient stress change in the FBG (Figure S5, Supporting Information). As shown in Figure 4e, our LNOFFPF, driven by a 1.52 MHz AC voltage, effectively records the transient events after the demodulation algorithm (red curve), which closely matches the data collected by the acquisition system (blue curve). It can be seen that the center wavelength of the FBG redshifts ≈6 nm at the moment when the FBG is straightened, and this redshift only occurs within ≈3.3 ms. By combining the FBG sensitivity (about 1.2 pm per $\mu\epsilon$) and the fiber's elastic modulus of (≈70 GPa), we calculated that the instantaneous stress at the fiber grid region is 3.5×10^8 N m^{-2}. Multiplying this stress by the cross-sectional area of the optical fiber gives an instantaneous tensile force of ≈4.29 N, which closely matches the theoretical tensile force of ≈4.07 N (see Supporting Information for details), highlighting the high-speed demodulation capability of the LNOFFPF in practical applications.

In similar sensing systems, the implementation of this spectral scanning approach for wavelength demodulation offers advantages such as high resolution, broad tuning range, and com-

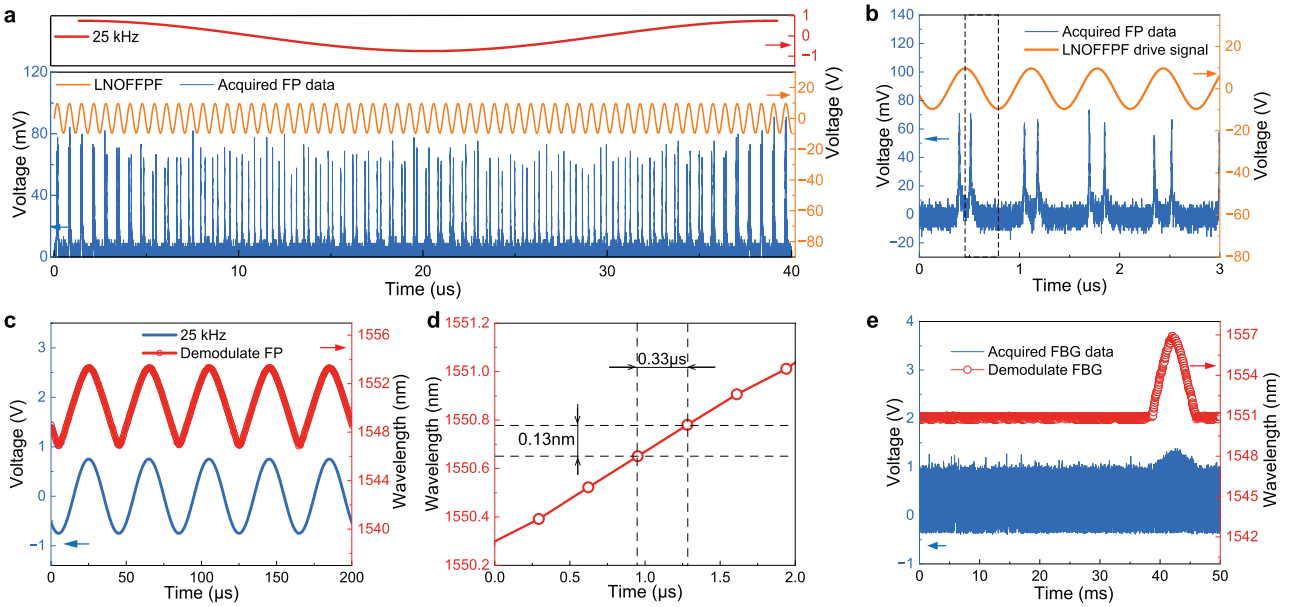

Figure 4. High-speed spectral signal measurement based on $LiNbO_3$-actuated OFFPF. a) Time domain display of high-speed spectral signal measured by LNOFFPF on PD. b) Relationship between driving voltage of LNOFFPF and high-speed spectral signal of FP filter scanned by LNOFFPF in the time domain. c) Demodulated high-frequency spectral signal versus original signal drive voltage. d) A close-up view of the demodulation of the FP filter. e) Transient strain sensed by FBG measured by spectrometer.

patibility with high-capacity distributed sensing demodulation. In the researches on the wavelength demodulation, the state of the art for spectrum scanning scheme achieve a tuning frequency of about 100 kHz, which is limited by the high mechanical and dielectric loss of PZT. In contrast, our strategy demonstrates remarkable advantages, particularly in terms of speed. With a scanning rate of 1.52 MHz, which is an order of magnitude higher than that of conventional PZT-based methods, it is well-positioned to meet the requirements of high-speed dynamic sensing scenarios. Moving forward, we aim to further expand the spectral scanning range of the LNOFFPF to enhance its demodulation capacity, enabling parallel demodulation across multiple wavelength channels.

3. Conclusion

In summary, we demonstrated a high-speed tunable OFFPF with enhanced integration, stability, improved tuning linearity, and superior repeatability. By enhancing the overall stiffness of the actuator's multilayer composite structure and employing an integrated design approach to minimize the load on the actuator, we have effectively realized its high-frequency potential for filtering applications. The assembly process of the LNOFFPF requires careful consideration of factors such as the elastic modulus, connection strength, and TEC of the connecting layer material, as well as the mitigation of creep effects. During bonding, it's essential to control parameters to avoid micro-cracks in the piezoelectric chip, which could lead to structural hysteresis and creep. Through the elaborate design and assembly, we achieve a 20 nm wavelength tuning range under an AC voltage of 1.52 MHz frequency and 60 Vpp amplitude. Its dynamic spectral measurement capability was demonstrated by monitoring the submicrosecond spectral signal variation from an actuated tunable FP filter and capturing instantaneous stress variations in an FBG. In future work, we aim to further enhance the filter's tuning range and frequency by optimizing the bonding process and minimizing acoustic energy leakage into the substrate using the present actuator configuration. This $LiNbO_3$-actuated fiber FP MHz-tunable filter we demonstrated is not only competitive in high-speed demodulation and multi-parameter real-time monitoring for fiber optic sensing, but also holds significant potential for use in areas such as optical coherence tomography (OCT) imaging, lidar, and optical frequency domain reflectometry (OFDR) ranging.

Supporting Information

Supporting Information is available from the Wiley Online Library or from the author.

Acknowledgements

H.T. and Y.X. contributed equally to this work. This research was funded by National Key R&D Program of China (2021YFA1401103), National Natural Science Foundation of China (62135007 and 62305153), Natural Science Foundation of Jiangsu Province (BK20243014 and SBK2023040245), Guangdong Basic and Applied Basic Research Foundation (2023B1515120011), and Innovation Program for Quantum Science and Engineering (2021ZD0300700), Natural Science Foundation of Guangdong Province (2514050001485).

Conflict of Interest

The authors declare no conflict of interest.

Data Availability Statement

The data that support the findings of this study are available from the corresponding author upon reasonable request.

Keywords

lithium niobite, megahertz-rate, piezoelectric, tunable fiber filters

Received: April 10, 2025
Revised: June 10, 2025
Published online: July 2, 2025

[1] C. Sun, Y. Yin, Z. Chen, Y. Ye, Y. Luo, H. Ma, L. Wang, M. Wei, J. Jian, R. Tang, H. Dai, J. Wu, J. Li, D. Zhang, H. Lin, L. Li, *PhotoniX* **2022**, *3*, 12.
[2] D. P. Karothu, G. Dushaq, E. Ahmed, L. Catalano, S. Polavaram, R. Ferreira, L. Li, S. Mohamed, M. Rasras, P. Naumov, *Nat. Commun.* **2021**, *12*, 1326.
[3] N. S. Makarov, K. Ramasamy, A. Jackson, A. Velarde, C. Castaneda, N. Archuleta, D. Hebert, M. R. Bergren, H. McDaniel, *ACS Nano* **2019**, *13*, 9112.
[4] P. Song, R. Wang, L. Loetgering, J. Liu, P. Vouras, Y. Lee, S. Jiang, B. Feng, A. Maiden, C. Yang, G. Zheng, *Light: Sci. Appl.* **2024**, *13*, 168.
[5] H. Im, S. Hong, Y. Lee, H. Lee, S. Kim, *Adv. Mater.* **2019**, *31*, 1807552.
[6] Y.-L. Xu, X.-H. Zhang, S. Zhu, S. Zhan, *Sci. Bull.* **2016**, *61*, 313.
[7] Q. Rong, X. Qiao, *J. Lightwave Technol* **2018**, *37*, 2502.
[8] W. Huang, W. Zhang, Y. Lu, Li, W. L, F. Li, *Opt. Express* **2018**, *26*, 10705.
[9] C. S. Shin, C. C. Chiang, *J. Chin. Inst. Eng.* **2005**, *28*, 985.
[10] H. Tsuda, J.-R. Lee, Y. Guan, *Smart Mater. Struct.* **2006**, *15*, 1429.
[11] J. Ang, H. C. H. Li, I. Herszberg, M. K. Bannister, A. P. Mouritz, *Int. J. Fatigue* **2010**, *32*, 762.
[12] C. A. R. Diaz, A. G. Leal-Junior, L. M. Avellar, P. F. C. Antunes, M. J. Pontes, C. A. Marques, A. Frizera, M. R. N. Ribeiro, *Sensors* **2019**, *19*, 2962.
[13] W. Zhang, F. Ren, Y. Li, B. Jin, W. Dai, *Photonic Sens.* **2018**, *8*, 270.
[14] W. Wang, R. Liang, Z. Zhou, Y. Zhang, X. Dong, *J. Am. Ceram. Soc.* **2022**, *105*, 279.
[15] Z. Li, H.-C. Thong, Y.-F. Zhang, Z. Xu, Z. Zhou, Y.-X. Liu, Y.-Y.-S. Cheng, S.-H. Wang, C. Zhao, F. Chen, K. Bi, B. Han, K. Wang, *Adv. Funct. Mater.* **2021**, *31*, 2005012.
[16] J.-M. Cha, S.-J. Ha, J.-h. Kim, H.-A. Cha, J.-J. Choi, B.-D. Hahn, K.-H. Cho, S.-Y. Yoon, C.-W. Ahn, *Ceram. Int.* **2023**, *49*, 264.
[17] C.-L. Dai, F.-Y. Xiao, C.-Y. Lee, Y.-C. Cheng, P.-Z. Chang, S.-H. Chang, *Mater. Sci. Eng.* **2004**, *384*, 57.
[18] H. Dong, M. Chen, H. Zhu, Y. Huang, Q. Ding, J. Feng, *Ceram. Int.* **2019**, *46*, 1883.
[19] W. Sheng, G. D. Peng, N. Yang, Y. Kang, D. Soeffker, *Mech. Syst. Signal Process.* **2020**, *142*, 106724.
[20] Z. M. Hu, Y. Su, J. Li, *Compos. Sci. Technol.* **2021**, *204*, 108649.
[21] K. P. Wong, H.-T. Kim, A. Wang, K. Kiger, J. H. Duncan, M. Yu, *Smart Mater. Struct.* **2020**, *29*, 125021.
[22] C. Saavedra, D. Pandey, W. Alt, H. Pfeifer, D. Meschede, *Opt. Express* **2021**, *29*, 974.
[23] D. V. Sabarianand, P. Karthikeyan, T. Muthuramalingam, *Mech. Syst. Signal Process.* **2020**, *140*, 106634.
[24] M.-S. Chae, J.-H. Koh, *Ceram. Int.* **2014**, *40*, 2551.
[25] T. W. Secord, H. H. Asada, *IEEE Trans. Rob.* **2010**, *26*, 993.
[26] Y. Shi, D. Kong, C. Zhang, *IEEE Sens. J.* **2022**, *22*, 20312.
[27] O. Atalar, R. Van Laer, A. H. Safavi-Naeini, A. Arbabian, *Nat. Commun.* **2022**, *13*, 1526.
[28] H. Yao, P. Zheng, S. Zhang, C. Hu, X. Fang, L. Zhang, D. Ling, H. Chen, X. Ou, *Nat. Commun.* **2024**, *15*, 5002.
[29] S. A. Mathews, A. C. Ehrlich, N. A. Charipar, *Sci. Rep.* **2020**, *10*, 15141.
[30] V. Y. Shur, I. S. Baturin, E. A. Mingaliev, D. V. Zorikhin, A. R. Udalov, E. D. Greshnyakov, *Appl. Phys. Lett.* **2015**, *5*, 106.
[31] A. Emad, R. Lu, M.-H. Li, Y. Yang, T. Wu, S. Gong, in *32nd IEEE Int. Conf. on Micro Electro Mechanical Systems (IEEE MEMS)*,Seoul, Korea (South),**2019**, pp. 282–285.
[32] Z.-D. Zhang, S.-Y. Yu, H. Xu, M.-H. Lu, Y.-F. Chen, *Adv. Mater.* **2024**, *36*, 2312861.
[33] J.-H. Song, J.-L. Huang, S. Wu, S.-C. Wang, J.-L. Ruan, D.-F. Lii, *Appl. Surf. Sci.* **2010**, *256*, 7156.
[34] M. Churaev, R. N. Wang, A. Riedhauser, V. Snigirev, T. Blésin, C. Möhl, M. H. Anderson, A. Siddharth, Y. Popoff, U. Drechsler, D. Caimi, S. Hönl, J. Riemensberger, J. Liu, P. Seidler, T. J. Kippenberg, *Nat. Commun.* **2023**, *14*, 3499.
[35] R. Wu, J. Lin, M. Wang, Z. Fang, W. Chu, J. Zhang, J. Zhou, Y. Cheng, *Opt. Lett.* **2019**, *44*, 4698.
[36] R. Zhuang, J. He, Y. Qi, Y. Li, *Adv. Mater.* **2022**, *35*, 2208113.
[37] H. Tong, Y. Xiong, H. Ding, Z. Chen, Z. Qin, W. Chen, J. Tang, S. Yu, F. Xu, *ACS Photonics* **2024**, *11*, 1574.
[38] G. Guo, S. Zhong, Q. Zhang, J. Zhong, D. Liu, *Sensors* **2023**, *23*, 7585.
[39] Y. Hu, X. Liang, W. Wang, *Sens. Actuators, A* **2017**, *258*, 74.
[40] D. Mao, J. Wang, H. Zhao, *Precis. Eng.* **2024**, *86*, 239.